

Tidal Calibration of Multicomponent Borehole Strainmeters and Validation of the Method Using Surface Waves

Norio Matsumoto (✉ n.matsumoto@aist.go.jp)

Geological Survey of Japan, AIST <https://orcid.org/0000-0002-7021-1773>

Osamu Kamigaichi

Japan Meteorological Business Support Center

Full paper

Keywords: in-situ calibration, multicomponent borehole strainmeters, oceanic tidal loading, calibration matrix, seismic strain wave

Posted Date: June 15th, 2021

DOI: <https://doi.org/10.21203/rs.3.rs-602970/v1>

License:   This work is licensed under a Creative Commons Attribution 4.0 International License.

[Read Full License](#)

1 **Tidal Calibration of Multicomponent Borehole Strainmeters and Validation of the**
2 **Method Using Surface Waves**

3 Author #1: Norio Matsumoto, Geological Survey of Japan, National Institute of
4 Advanced Industrial Science and Technology (AIST), AIST Tsukuba Central 7, 1-1-1
5 Higashi, Tsukuba, Ibaraki 305-8567, Japan, n.matsumoto@aist.go.jp

6 Author #2: Osamu Kamigaichi, Japan Meteorological Business Support Center, To-nen
7 Bld., 3-17 Kanda-Nishikicho, Chiyoda-ku, Tokyo, 101-0054, Japan,
8 kamigaichi@jmbsec.or.jp,

9 and Geological Survey of Japan, National Institute of Advanced Industrial Science and
10 Technology (AIST), AIST Tsukuba Central 7, 1-1-1 Higashi, Tsukuba, Ibaraki 305-
11 8567, Japan

12

13 Corresponding author: Norio Matsumoto

14

15

16 **Abstract**

17 We conducted in-situ calibration of fifteen multicomponent borehole strainmeters
18 deployed in and around the expected focal zones of the Nankai megathrust earthquake.
19 The in-situ calibration method compares tidal strain observed by the borehole
20 strainmeters with predicted tidal strains from the solid Earth's tide and oceanic tidal
21 loading. Then we obtained a calibration matrix to transfer observed strain data to the
22 regional strain field. We estimated the oceanic tidal loading accurately using a Green's
23 function, which takes the depth of deployment into consideration. We calculated four
24 sets of calibration matrices using combinations of any three of a group of four gauges as
25 well as a calibration matrix using all four gauges. The estimated calibration matrix was
26 validated by comparing observed seismic strain waves after applying the calibration
27 matrix with theoretical seismic strain waves excited by the 2010 Chile earthquake (Mw
28 8.8). The in-situ calibration was found to be appropriate for all eleven Ishii-type
29 borehole strainmeters and for one of the four Gladwin Tensor Strainmeters (GTSMs). It
30 was also effective with respect to two shear strains for two of the other three GTSMs.

31

32 **Keywords:** in-situ calibration, multicomponent borehole strainmeters, oceanic tidal
33 loading, calibration matrix, seismic strain wave

34 **Main Text**

35 1. Introduction

36 The Geological Survey of Japan (GSJ), an arm of the National Institute of Advanced
37 Industrial Science and Technology (AIST), constructed fourteen groundwater and
38 crustal deformation observatories in and around the Kii peninsula and the island of
39 Shikoku for the purpose of research aimed at predicting the anticipated Nankai
40 megathrust earthquake (Itaba *et al.*, 2010; Koizumi, 2013). In this region, the Philippine
41 Sea Plate subducts beneath the continental plate, and Tonankai and Nankai earthquakes
42 have recurred every 100-150 years (Ando, 1975). In the transitional zone of this plate
43 interface, slow slip events (SSEs) have been observed (Obara *et al.*, 2004; Obara &
44 Hirose, 2006; Sekine *et al.*, 2010). The GSJ deployed a borehole strainmeter at each
45 observatory. Four of the fourteen borehole strainmeters are Gladwin Tensor
46 Strainmeters (GTSMs, Gladwin, 1984), and the others are Ishii-type strainmeters (Ishii
47 *et al.*, 2002; Asai *et al.*, 2009). The borehole strainmeters consist of four horizontal
48 extensometers with different orientations; these are highly sensitive, measuring less than
49 one nano-strain, which allows us to detect strain signals associated with the SSEs
50 occurring near these observatories.

51 These strainmeters are deployed with expansive grout at the bottom of the boreholes.

52 The observed strain data differs from the strain in the surrounding rock because the elastic
53 moduli of the host rocks are not the same as those of the strainmeters due to the
54 combination of host rocks, expansive grout and strainmeter housing at the deployment
55 depth. Therefore, the strainmeters must be calibrated in-situ in to accurately estimate the
56 strain in the surrounding rock.

57 Several methods for calibrating multi-component borehole strainmeters have been
58 proposed. King *et al.* (1979) first proposed the idea of site correction for strainmeters
59 using tides and Rayleigh waves. Gladwin & Hart (1985) reported the analytical response
60 of borehole strainmeters to areal and shear strain in the surrounding rock for the case of
61 an isotropic medium. Hart *et al.* (1996), Roeloffs (2010) and Hodgkinson *et al.* (2013)
62 obtained coupling coefficients determined by comparing the linear response of observed
63 strain due to the Earth's tides to the theoretical strain estimated using the SPOTL software
64 package (Agnew, 1996; 1997) for each borehole strainmeter.

65 We applied in-situ tidal calibration methods based on Roeloffs (2010) for the
66 observed strain using a calibration matrix determined by the response of the AIST
67 borehole strainmeter to the Earth's tides. We took the depth of deployment into
68 consideration by using the modified GOTIC2 program (Kamigaichi *et al.*, 2020;
69 Kamigaichi *et al.*, 2021) when we calculated the theoretical tidal strain precisely. The

70 estimated calibration matrix was validated using a coupling matrix and by comparing
71 the theoretical and observed long-period seismic surface waves excited by the 2010
72 Chile (Maule) earthquake (Mw 8.8).

73

74 2. Observatories and deployed borehole strainmeters

75 The fourteen observatories have been in place since 2007 (Fig. 1 and Table 1) (Itaba
76 *et al.*, 2010; Koizumi, 2013). Each consists of three wells whose depths are about 30 m,
77 200 m and 600 m (Fig. 2). One borehole strainmeter is deployed at the bottom of either
78 the 600-m well or the 200-m well at each observatory. A groundwater level sensor and
79 groundwater temperature sensor are deployed in each well, and each observatory is
80 equipped with an atmospheric pressure sensor and rain gauge. There are also static
81 Global Navigation Satellite System (GNSS) stations in some observatories (Itaba *et al.*,
82 2010; Koizumi, 2013). All station data except GNSS data are transferred to the GSJ in
83 real time.

84 The Ishii-type borehole strainmeters in ten of the observatories are equipped with
85 four-component horizontal strain gauges, one vertical strain gauge, a three-component
86 seismometer and a three-component magnetometer (Ishii *et al.*, 2002; Asai *et al.*, 2009).
87 These are deployed at the bottom of the 600-m wells. The GTSM units consist of four

88 horizontal strain gauges, and they are deployed at the bottom of the 200-m wells. The
89 relative orientations of the four horizontal strain gauges are 45, 90 and 135 degrees from
90 CH1 (Fig. 3). The exact deployment depth and geology at that depth are shown in
91 Table 1 for each strainmeter. In 2004, an Ishii-type borehole strainmeter was deployed
92 at observatory station TYE, which has a 267-m well (Fig. 1, Table 1). In total, data from
93 eleven Ishii-type borehole strainmeters (including the one at TYE) and four GTSMs are
94 analyzed in this paper.

95 The resolution of the Ishii-type borehole strainmeters is less than 1 nano-strain, and
96 that of the GTSMs is at least 0.1 nano-strain (Gladwin, 1984; Ishii *et al.*, 2002; Asai *et*
97 *al.*, 2009). These strainmeters continuously record strain data at a rate of 40 samples per
98 second at station TYE and 20 samples per second at the other observatories. Data is
99 decimated to hourly samples for tidal analysis and one sample per second for analysis of
100 seismic surface waves.

101

102 3. Tidal and atmospheric responses of the borehole strainmeter data

103 Observed tidal responses of the M_2 and O_1 constituents for each gauge of the borehole
104 strainmeters were extracted using the computer program BAYTAP-G (Tamura *et al.*,
105 1991). Seventeen to 24 months of continuous strain data were analyzed to extract the

106 M_2 and O_1 tidal responses for 14 of the 15 borehole strainmeters. For the strainmeter at
107 station HGM, 2.5-13 months of data were used because of repeating abrupt steps in the
108 continuous strain data. The amplitude responses, phase shifts and RMSEs for the M_2
109 and O_1 constituents are shown in Table 2. $\text{Re}(e_i^{M_2})$, $\text{Im}(e_i^{M_2})$, $\text{Re}(e_i^{O_1})$ and
110 $\text{Im}(e_i^{O_1})$ ($i = 1, \dots, 4$) are calculated as inputs for the calibration (Section 5, Appendix
111 B) using the observed amplitude response and phase shift for the M_2 and O_1 constituents
112 shown in Table 2.

113 The atmospheric responses of the 15 borehole strainmeters, extracted using BAYTAP-
114 G, are also shown in Table 2. The atmospheric responses range from -0.109 to -1.492
115 nano-strain/hPa for 43 of the 44 gauges in the eleven Ishii-type borehole strainmeters
116 (all but gauge 2 at station HGM), while the atmospheric responses for the 16 gauges of
117 the GTSMs range from -1.95 to -4.454 nano-strain/hPa.

118

119 4. Predicted tidal strain considering deployment depth

120 As shown in Table 3, we calculated the theoretical areal, pure shear and engineering
121 shear strains, ϵ_A^F , ϵ_D^F and ϵ_S^F , respectively, caused by the solid Earth (body) tide, E ,
122 oceanic tidal loading, O , and their sum, $E + O$, using the modified GOTIC2 program
123 (Kamigaichi *et al.*, 2020; Kamigaichi *et al.*, 2021), where the areal strain, shear strain as

124 a differential extension (pure shear strain) and engineering shear strain of the formation
125 strain field defined by Roeloffs (2010) are expressed as $\varepsilon_A^F = \varepsilon_{xx}^F + \varepsilon_{yy}^F$, $\varepsilon_D^F = \varepsilon_{xx}^F - \varepsilon_{yy}^F$
126 and $\varepsilon_S^F = 2\varepsilon_{xy}^F$, respectively. Here, the x-axis represents east-west and the y-axis
127 represents north-south. The term “formation strain” in Roeloffs (2010) and the present
128 paper is used in the same way that “remote strain” in Hart *et al.* (1996) and “regional
129 strain” in Hodgkinson *et al.* (2013) are used.

130 In addition, we used latitudes and longitudes based on the Tokyo datum (Matsumura *et*
131 *al.*, 2004) in Table 1 for the modified GOTIC2 because the Japanese coastline in the
132 modified GOTIC2 is based on the Tokyo datum (Kamigaichi *et al.*, 2020; Kamigaichi *et*
133 *al.*, 2021).

134

135 5. Calibration Method

136 In order to estimate the formation strain field from the measurement outputs of the
137 borehole strainmeters, we calculated an appropriate coupling matrix using the modeled
138 Earth’s tides. To estimate the coupling matrix, we applied the relationship between the
139 borehole strainmeter outputs and the formation strain field proposed by Roeloffs (2010).
140 Details of the method used to calculate the coupling matrix are given in Appendix A.

141

142 6. Results of in-situ tidal calibration

143 We estimated five sets of calibration matrices using all four strain gauges \mathbf{C}_{1234} and
144 the combinations of any three of the four gauges discussed earlier, \mathbf{C}_{123} , \mathbf{C}_{124} , \mathbf{C}_{134}
145 and \mathbf{C}_{234} . In order to obtain optimal calibration matrices for each borehole strainmeter,
146 we set the following constraints: $-0.5 \leq C^i \leq 4$, $0.1 \leq D^i \leq 6$, and $H^i = 0$ ($i =$
147 $1, \dots, 4$) in equations (A2) and (B4).

148 Table 4 shows the five calibration matrices \mathbf{C} , the coupling matrices \mathbf{K} and \mathbf{D} derived
149 from equation (B2), D_{matrix} calculated from equation (A8) and the perturbation matrix
150 \mathbf{P} (from equation (A9)). The results for the Ishii-type borehole strainmeters and
151 GTSMs are described separately below.

152

153 6-1. Ishii-type borehole strainmeters

154 The values of \mathbf{D} for the eleven Ishii-type borehole strainmeters are relatively small
155 (0.11 - 0.58) except at station TYE ($\mathbf{D} = 0.52$ to 1.10). D_{matrix} , which is the difference
156 between the coupling matrices for the four gauges, is the difference between the four-
157 gauge coupling matrix (\mathbf{K}_{1234}) and each of the other coupling matrices (\mathbf{K}_{123} , \mathbf{K}_{124} ,
158 \mathbf{K}_{134} or \mathbf{K}_{234}) for each observatory. It ranges from 0.11 to 0.37. The four values of
159 D_{matrix} for each observatory differ only slightly, indicating that each observatory's five

160 calibration matrices are plausible and self-consistent.

161 Next, we focus on the coupling matrix \mathbf{K} and the perturbation matrix \mathbf{P} to discuss
162 the borehole strainmeter calibration results. The value of k_{11} , the isotropic coupling
163 coefficient for the areal strain, ranges from 0.91 to 1.92, and the mean and standard
164 deviation of the fifty-five k_{11} values are 1.28 ± 0.28 . The values of k_{22} and k_{33} ,
165 the isotropic coupling coefficients for the two shear strains, range from 1.23 to 6.30 and
166 1.15 to 5.98, respectively. The mean and standard deviations of the fifty-five k_{22} and
167 k_{33} values are 3.29 ± 1.29 and 2.94 ± 1.11 , respectively. As mentioned previously,
168 typical values for the isotropic coupling coefficients are $k_{11} = 1.5$, and $k_{22} = k_{33} = 3$
169 when the formation is homogeneous and isotropic (Gladwin & Hart, 1985; Hart *et al.*,
170 1996; Roeloffs, 2010). The mean values of k_{11} , k_{22} and k_{33} are mostly close to the
171 typical values, while the standard deviations of k_{22} and k_{33} are slightly larger. The
172 means and standard deviations of k_{22}/k_{11} and k_{33}/k_{11} are 2.55 ± 0.75 and $2.28 \pm$
173 0.65 , respectively, while a typical theoretical value is 2. Since the standard deviations
174 of k_{22}/k_{11} and k_{33}/k_{11} are much smaller than the standard deviations of k_{22} and
175 k_{33} , the large standard deviations of k_{22} and k_{33} are dependent on the deployment
176 site.

177 The cross-coupling coefficients, k_{12} , k_{13} , k_{21} , k_{23} , k_{31} and k_{32} , range from -

178 0.82 to 3.26. The cross-coupling perturbation coefficients, p_{12} , p_{13} , p_{21} , p_{23} , p_{31}
179 and p_{32} range from -0.83 to 0.89. Of the 330 perturbation coefficients in the 55
180 matrices, 76% are within ± 0.2 , which are not unexpected values (Berger & Beaumont,
181 1976; Sato & Harrison, 1990; Tamura *et al.*, 1991; Hart *et al.*, 1996). Of particular note,
182 23 of the 30 perturbation coefficients for the five perturbation matrices for station MUR
183 have absolute values greater than 0.2, whereas more than 22 of the 30 perturbation
184 coefficients are within ± 0.2 in the other ten Ishii-type borehole strainmeters at stations
185 TYS, TYE, ANO, MYM, ICU, HGM, KST, SSK, TSS and UWA. These results show
186 that the calibration matrices at MUR have a relatively large cross-coupling perturbation
187 compared to the small perturbations in the matrices for the other ten observatories.

188 The observatories at stations KST, ICU, MUR, SSK and TSS have Ishii-type
189 borehole strainmeters and are located less than 1 km from the coastline (Fig. 1; Table 3).
190 The predicted M_2 and O_1 tidal strains caused by the ocean loading at these observatories
191 are approximately as large as the body tide strain (Table 3). The predicted ocean loading
192 tidal strains calculated using the conventional Green's function are very different from
193 those calculated using a Green's function that takes deployment depth into
194 consideration (Kamigaichi *et al.*, 2021). The values of D and D_{matrix} for the five
195 observatories range from 0.1672 to 0.532 and 0.1404 to 0.3736, respectively, and all lie

196 within the values of D and $D_{\text{matrix}i}$ for the other six observatories located farther away
197 from the coastline. Moreover, the means and standard deviations of the values of k_{11} ,
198 k_{22}/k_{11} and k_{33}/k_{11} for stations KST, ICU, MUR, SSK and TSS are 1.35 ± 0.29 ,
199 1.97 ± 0.60 and 1.74 ± 0.49 , respectively. These values are close to the typical values
200 noted above. The perturbation coefficients for stations KST, ICU, SSK and TSS are also
201 quite similar to those for the other six observatories located more than 1 km from the
202 coastline. These results show that the in-situ tidal calibration performed in this study is
203 effective for multi-component borehole strainmeters at observatories less than 1 km
204 from the coast.

205

206 6-2. GTSM

207 We estimated the calibration matrices \mathbf{C}_{1234} , \mathbf{C}_{123} , \mathbf{C}_{124} , \mathbf{C}_{134} and \mathbf{C}_{234} for the
208 GTSM at station ITA using equations (B2) and (B4). As shown in Table 4, D and
209 D_{matrix} are similar to those for the eleven Ishii-type borehole strainmeters, and the
210 isotropic coupling coefficients k_{11} , k_{22} , and k_{33} in the five coupling matrices \mathbf{K}
211 range from 0.850 to 1.032, 3.04 to 3.994, and 2.982 to 3.325, respectively. Of the 30
212 cross-coupling perturbation coefficients, 27 are within ± 0.2 (Table 4). These results
213 show that the estimated calibration matrices are plausible.

214 At the other three GTSMs (at stations MAT, ANK and KOC), we estimated \mathbf{C}_{1234}
215 using equations (A1) and (A2), which consider anisotropic coupling (Roeloffs, 2010).
216 The values of D and D_{matrix} for those three observatories are as large as those for the
217 Ishii-type borehole strainmeters. However, the areal isotropic coefficients k_{11} for
218 stations MAT and ANK are less than 0.5, and 11 of the 18 cross-coupling perturbation
219 coefficients in the three \mathbf{P}_{1234} matrices have absolute values greater than 0.2. Two of
220 the coefficients are greater than 0.9. These results suggest that the three GTSMs at
221 stations MAT, ANK and KOC have large vertical and shear coupling as Roeloffs (2010)
222 described.

223

224 7. Validation of the in-situ tidal calibration using long-period seismic surface waves

225 Strainmeters often observe strain oscillations associated with large earthquakes
226 (e.g., Park *et al.*, 2008; Zürn *et al.*, 2015). The fifteen borehole strainmeters also
227 recorded long-period seismic surface waves excited by the 2010 Chile (Maule)
228 earthquake (Mw 8.8). Kitagawa *et al.* (2011) showed that the amplitude spectra of the
229 observed volumetric strain is larger than the noise amplitude spectra at about 10 – 1,000
230 s in ANO.

231 In order to validate the in-situ tidal calibration coefficients for the strainmeters as

232 described in Section 6, we compared two kinds of observed seismic strain waves with
233 synthetic strain waves. One set of observed strain waves was obtained by applying the
234 calibration matrices in Table 4 to the observed strain data, e_1, e_2, e_3 and e_4 , hereafter
235 termed observed strain after calibration, ε_A^C , ε_D^C and ε_S^C . We also used strain waves ε_A^I ,
236 ε_D^I and ε_S^I , that had been geometrically transformed from the observed strain data using
237 the values of \mathbf{O}^+ from equation (A5) – (A7), hereafter referred to as observed strain
238 without calibration. In these procedures, five different sets of observed strain waves
239 with and without calibration were calculated for each borehole strainmeter, that is, strain
240 waves produced by all four strain gauges and by the three-gauge combinations. The
241 observed strain data was reduced to one sample per second from its original 20-40 Hz
242 form.

243 Theoretical seismic strain waves, ε_A^F , ε_D^F and ε_S^F were calculated by summing
244 spheroidal and toroidal modes (periods from 45 to 3000 s) using the computer program
245 described in Appendix C, based on the normal mode theory reported by Gilbert &
246 Dziewonski (1975) and Dziewonski *et al.* (1981). We used the source parameters for
247 the earthquake from the Global CMT Web Page (Ekström *et al.*, 2012) to calculate the
248 theoretical strain waves.

249 After bandpass filtering in the 300-1000 s range for the two observed strain waves

250 and the theoretical strain waves, we compared the observed and theoretical strain waves
251 with respect to the three horizontal strain components ε_A , ε_D and ε_S . Comparisons of
252 the observed strain waves calculated for all four strain gauges with the theoretical strain
253 waves for the fifteen borehole strainmeters are shown in Figures 6a, 6b, and 6c. The
254 four sets of observed strain waves obtained using the 3-gauge groupings described
255 earlier and the theoretical strain waves for 12 of the 15 borehole strainmeters (excluding
256 the GSTMs at stations ANK, KOC and MAT) are shown in Figures S1a –S1l in the
257 Supplemental Material. There are several gaps in the observed strain waves at station
258 UWA in Figures 4b and S1k because of missing observations.

259 7-1. Ishii-type borehole strainmeters

260 We compared the observed strain waves without calibration using all four gauges,
261 ε_A^I , ε_D^I and ε_S^I , to the theoretical strain waves, ε_A^F , ε_D^F and ε_S^F , respectively, for each
262 borehole strainmeter (Figs. 4a and 4b). The value of ε_A^I is about equal to or slightly
263 larger than ε_A^F , while ε_D^I and ε_S^I are much larger than ε_D^F and ε_S^F , respectively. Note
264 that the phases of ε_A^I , ε_D^I , ε_S^I and ε_A^F , ε_D^F , ε_S^F , respectively, are the same for all the
265 borehole strainmeters. This shows that there is no strong inhomogeneous or anisotropic
266 coupling among ε_A^I , ε_D^I , and ε_S^I . Next, we compared ε_A^C , ε_D^C and ε_S^C with ε_A^I , ε_D^I , and
267 ε_S^I as well as ε_A^F , ε_D^F , and ε_S^F , respectively. The amplitude of ε_A^C is smaller than that

268 of ε_A^I and closer to that of ε_A^F at stations TYS, ANO, MYM, KST, HGM, SSK and
269 UWA. The amplitude of ε_A^C is similar to that of ε_A^I for the other four strainmeters. The
270 amplitudes of ε_D^C and ε_S^C dropped significantly after the calibration coefficients were
271 applied, and the values of ε_D^C and ε_D^F became similar for all the strainmeters. The
272 amplitude of ε_S^C came closer to that of ε_S^F than that of ε_S^I .

273 In Section 6-1, the standard deviations of k_{22} and k_{33} in the 55 coupling matrices
274 \mathbf{K} were noted as being relatively large. After validation, the amplitudes of ε_D^I and ε_S^I
275 were found to be large at borehole strainmeters that had large values of k_{22} and k_{33} ,
276 respectively. In fact, k_{22} and k_{33} are larger than 6.0 at station MYM, and the
277 amplitudes of ε_D^I and ε_S^I are over 50 and over 30 nano-strain, respectively. Since ε_D^C
278 and ε_S^C dropped to appropriate levels after the calibration matrices were applied for all
279 eleven Ishii-type borehole strainmeters, the large standard deviations of k_{22} and k_{33}
280 were shown to be dependent on the deployment site.

281 The four sets of observed strain waves produced by the 3-gauge combinations (Figs.
282 S1a –S1k) have characteristics similar to the strain waves using all four gauges. This is
283 shown by comparing them with the theoretical strain waves for all the Ishii-type
284 borehole strainmeters except for the one at station MUR (Fig. S1h).

285 At station MUR, two of the four ε_A^C values and three of the four ε_D^C values did not

286 improve after the tidal calibration, and only two gauge combinations, 1, 2, 4 and 1, 2, 3,
287 4 showed plausible calibrations when we attempted to validate them using strain waves.
288 One reason for this could be that the calibration matrices for combinations 1, 2, 3; 1,3,
289 4; and 2, 3, 4 have large cross-coupling perturbation coefficients as shown in Table 4.

290 The validation using strain waves shows that tidal calibration is plausible for Ishii-
291 type borehole strainmeters at stations less than 1 km from the coastline (KST, ICU,
292 MUR, SSK and TSS) as well as for strainmeters deployed landward, except for the
293 gauge combinations at station MUR described above. These results indicate that the in-
294 situ tidal calibration method presented in this paper is appropriate and effective.

295

296 7-2. GTSMs

297 We compared the observed strain waves after calibration, ϵ_A^C , ϵ_D^C , and ϵ_S^C to ϵ_A^I , ϵ_D^I ,
298 and ϵ_S^I as well as ϵ_A^F , ϵ_D^F , and ϵ_S^F , respectively, for each of the five gauge
299 combinations for the GTSM at station ITA and using all four gauges of the GTSMs at
300 stations ANK, KOC and MAT (Figs. 4c and S11).

301 After the tidal calibration of the GTSM at station ITA, the amplitudes of the ϵ_A^C
302 combinations came slightly closer to the values of ϵ_A^F for all five gauge combinations
303 except 1, 2, and 4. The amplitudes of ϵ_D^C and ϵ_S^C were significantly lower than those of

304 ε_D^I and ε_S^I and approached ε_D^F and ε_S^F , respectively, for all five gauge combinations.

305 This shows that tidal calibration for the GTSM at ITA is plausible.

306 The amplitudes of ε_D^C and ε_S^C at stations KOC and MAT came much closer to those
307 of ε_D^F and ε_S^F than to ε_D^I and ε_S^I after applying the tidal calibration. However, the
308 amplitude of ε_A^C was underestimated at KOC and overestimated at MAT after the tidal
309 calibration. One reason for this is that the ε_A^I amplitudes were significantly smaller
310 than the ε_A^F amplitudes at stations KOC and MAT because of the vertical coupling
311 noted in Roeloffs (2010). Indeed, GTSMs have much larger sensitivity to atmospheric
312 pressure than the Ishii-type strainmeters described in Section 3. This shows that the tidal
313 calibration in this paper is effective for ε_D and ε_S , but that another calibration method
314 is needed for ε_A at stations like MAT and KOC.

315 The values of ε_A^C , ε_D^C , and ε_S^C did not improve for the GTSM at ANK after tidal
316 calibration. There is, however, no phase shift between the strain waves without tidal
317 calibration ε_A^I , ε_D^I , ε_S^I and the theoretical strain waves ε_A^F , ε_D^F , ε_S^F . Thus, another
318 method using strain waves could be used to calibrate the GTSM at ANK.

319

320 8. Conclusions

321 We performed in-situ tidal calibration of eleven Ishii-type borehole strainmeters and

322 four GTSMs, each equipped with four gauges in a horizontal plane. The tidal calibration
323 method is based on Roeloffs (2010), comparing observed tidal strains with theoretical
324 tidal strains. By applying Green's functions that account for deployment depth in our
325 ocean tidal loadings, we were able to estimate precise theoretical tidal strains near the
326 coast. We conducted in-situ calibration of five combinations of strain gauges for each
327 borehole strainmeter. After validation using long-period seismic strain waves excited by
328 the 2010 Chile earthquake, we confirmed that all five calibration matrices for ten of the
329 Ishii-type borehole strainmeters and one of the GTSMs are appropriate. Two calibration
330 matrices for the strainmeter at station MUR and calibration matrices for two shear
331 strains for the GTSMs at stations KOC and MAT were also effective.

332 There are two problems with in-situ tidal calibration of multi-component borehole
333 strainmeters, as pointed out by Hodgekinson *et al.* (2013). One is that there are large
334 misfits between the observed and predicted tidal strains within a few kilometers of the
335 coastline, and the other concerns the method of validating the tidal calibration. It is
336 notable that we were able to solve these problems using the methods applied here.

337 The borehole strain data after tidal calibration will contribute to a detailed analysis of
338 short-term slow slip events occurring in and around the fifteen borehole strainmeter
339 observatories, as already seen in Obara *et al.* (2004) and Sekine *et al.* (2010).

340 **Declarations**

341 **The authors need to provide the following declarations.**

342

343 **Availability of data and materials**

344 All datasets described in this article are available upon request.

345

346 **Competing interests**

347 Both authors declare that they have no competing interests.

348

349 **Funding**

350 The observatories were constructed by the grant-in-aid of facilities expense by Ministry
351 of Economy, Trade and Industry (METI). This work was partly done as the research
352 project of the Research Institute of Earthquake and Volcano Geology, AIST.

353

354 **Authors' contributions**

355 N. Matsumoto obtained the borehole strainmeter data, calculated calibration matrices
356 for strainmeter data at the 15 observatories and wrote the manuscript except for
357 Appendix C. O. Kamigaichi made the program `synthe_me` for the calculation of the

358 synthetic horizontal strain tensors, and wrote Appendix C. Both authors approved the
359 final manuscript.

360

361 **Acknowledgments**

362 We acknowledge T. Kiguchi, Y. Kitagawa, S. Itaba, T. Ochi, T. Ookawa, N. Koizumi and
363 M. Takahashi for data acquisition and maintenance of the groundwater and crustal
364 deformation observatories. We are grateful to Prof. Duncan Agnew whose comments
365 helped improve and clarify the manuscript. The GMT software package (Wessel & Smith,
366 1998) was used to prepare some of the figures. The catalog of slow earthquakes in this
367 study was produced by the Japan Meteorological Agency, in cooperation with the
368 Ministry of Education, Culture, Sports, Science and Technology.

369

370 Appendix A: Detailed method to calculate the coupling matrix

371 We assume an x-y coordinate system using east-west as the x-axis and north-south as
 372 the y-axis. $\varphi_1, \varphi_2, \varphi_3$ and φ_4 are the angles of gauges 1, 2, 3 and 4 from the x-axis,
 373 respectively, measured counterclockwise. The outputs of gauges 1, 2, 3 and 4, written as
 374 e_1, e_2, e_3 and e_4 , respectively, are:

$$375 \begin{pmatrix} e_1 \\ e_2 \\ e_3 \\ e_4 \end{pmatrix} = \mathbf{C} \begin{pmatrix} \varepsilon_A^F \\ \varepsilon_D^F \\ \varepsilon_S^F \end{pmatrix}, \quad (\text{A1})$$

$$376 \mathbf{C} = \begin{pmatrix} C^1 & (D^1 \cos 2\varphi_1 - H^1 \sin 2\varphi_1) & (D^1 \sin 2\varphi_1 + H^1 \cos 2\varphi_1) \\ C^2 & (D^2 \cos 2\varphi_2 - H^2 \sin 2\varphi_2) & (D^2 \sin 2\varphi_2 + H^2 \cos 2\varphi_2) \\ C^3 & (D^3 \cos 2\varphi_3 - H^3 \sin 2\varphi_3) & (D^3 \sin 2\varphi_3 + H^3 \cos 2\varphi_3) \\ C^4 & (D^4 \cos 2\varphi_4 - H^4 \sin 2\varphi_4) & (D^4 \sin 2\varphi_4 + H^4 \cos 2\varphi_4) \end{pmatrix}, \quad (\text{A2})$$

377 where, $C^1 - C^4$ are the areal coupling coefficients for the gauges, $D^1 - D^4$ are
 378 the shear coupling coefficients, and $H^1 - H^4$ are the coupling coefficients for
 379 nonuniformity and/or anisotropy for gauges 1 – 4, respectively. In this study we applied
 380 equation (A2) with H^1, H^2, H^3 and $H^4 = 0$ to calibrate all eleven Ishii-type borehole
 381 strainmeters and one GTSM (at station ITA). In this case, there are eight unknown
 382 parameters ($C^1 - C^4$ and $D^1 - D^4$). To calibrate the three GTSMs at stations MAT,
 383 ANK and KOC, we applied equation (A2) with nonzero values for $H^1 - H^4$. In this case
 384 there are 12 unknown parameters ($C^1 - C^4, D^1 - D^4$ and $H^1 - H^4$). The
 385 unknown parameters in matrix \mathbf{C} are determined using the method in Appendix B.

386 The coupling matrix \mathbf{K} represents the relationship between the formation strain field

387 and the strains ε_A^I , ε_D^I and ε_S^I measured by the instruments (Hart *et al.*, 1996):

$$388 \quad \begin{pmatrix} \varepsilon_A^I \\ \varepsilon_D^I \\ \varepsilon_S^I \end{pmatrix} = \mathbf{K} \begin{pmatrix} \varepsilon_A^F \\ \varepsilon_D^F \\ \varepsilon_S^F \end{pmatrix} . \quad (\text{A3})$$

389 \mathbf{K} is a 3×3 matrix given by:

$$390 \quad \mathbf{K} = \begin{pmatrix} k_{11} & k_{12} & k_{13} \\ k_{21} & k_{22} & k_{23} \\ k_{31} & k_{32} & k_{33} \end{pmatrix} \quad (\text{A4})$$

391 For four-component strain gauges, the orientation matrix, \mathbf{O} , is

$$392 \quad \mathbf{O} = \frac{1}{2} \begin{pmatrix} 1 & \cos 2\varphi_1 & \sin 2\varphi_1 \\ 1 & \cos 2\varphi_2 & \sin 2\varphi_2 \\ 1 & \cos 2\varphi_3 & \sin 2\varphi_3 \\ 1 & \cos 2\varphi_4 & \sin 2\varphi_4 \end{pmatrix} \quad (\text{A5})$$

393 for any three of the four gauges ($i, j, k = 1, 2, 3$ or 4):

$$394 \quad \mathbf{O} = \frac{1}{2} \begin{pmatrix} 1 & \cos 2\varphi_i & \sin 2\varphi_i \\ 1 & \cos 2\varphi_j & \sin 2\varphi_j \\ 1 & \cos 2\varphi_k & \sin 2\varphi_k \end{pmatrix} \quad (\text{A6})$$

395 \mathbf{K} is obtained as follows:

$$396 \quad \mathbf{K} = \mathbf{O}^+ \mathbf{C} , \quad (\text{A7})$$

397 where \mathbf{O}^+ is the Moore-Penrose generalized inverse of \mathbf{O} (Roeloffs, 2010).

398 The diagonal components of \mathbf{K} represent the coupling coefficients for the areal strain

399 (k_{11}), pure shear strain (k_{22}), and engineering shear strain (k_{33}) between the formation

400 strain field and the strain measured by the instruments. The off-diagonal components of

401 \mathbf{K} represent the cross-coupling of the areal strain and two of the shear strain components

402 of the instrumentally measured formation strain field (Hart *et al.*, 1996). If the

403 formation is isotropic and homogenous, the off-diagonal components k_{12} , k_{13} , k_{21} ,
404 k_{23} , k_{31} , and $k_{32} = 0$ and typical values of the diagonal components are $k_{11} = 1.5$
405 and $k_{22} = k_{33} = 3$ (Gladwin & Hart, 1985; Hart *et al.*, 1996; Roeloffs, 2010). The
406 five coupling matrices, \mathbf{K}_{1234} , \mathbf{K}_{123} , \mathbf{K}_{124} , \mathbf{K}_{134} and \mathbf{K}_{234} are calculated using
407 equation (A3) for each strainmeter using all four gauges and combinations of three of
408 the four gauges. In order to quantify the difference between \mathbf{K}_{1234} and one of the other
409 coupling matrices, we calculated a parameter D_{matrix} as follows:

$$410 \quad D_{\text{matrix}} = \left\| \frac{\mathbf{K}_{ijk} - \mathbf{K}_{1234}}{9} \right\|, \quad (\text{A8})$$

411 where ' $\| \cdot \|$ ' is the Euclidean norm, and $i, j, k = 1, 2, 3$ or 4 .

412 The off-diagonal components of \mathbf{K} , k_{12} , k_{13} , k_{21} , k_{23} , k_{31} and k_{32} , which are
413 referred to as the cross-coupling coefficients (Hart *et al.*, 1996), are evaluated by the
414 following perturbation matrix, \mathbf{P} .

$$415 \quad \mathbf{P} = \begin{pmatrix} p_{11} & p_{12} & p_{13} \\ p_{21} & p_{22} & p_{23} \\ p_{31} & p_{32} & p_{33} \end{pmatrix}$$

$$416 \quad = \begin{pmatrix} 1 & k_{12}/k_{11} & k_{13}/k_{11} \\ k_{21}/k_{22} & 1 & k_{23}/k_{22} \\ k_{31}/k_{33} & k_{32}/k_{33} & 1 \end{pmatrix}. \quad (\text{A9})$$

417

418 Appendix B Method for determining matrix **C**

419 The eight or twelve unknown parameters in matrix **C** in section 5 can be estimated
 420 using the tidal responses for the M₂ and O₁ components measured from the outputs of
 421 gauges 1 – 4 and modeled tidal responses ε_A^F , ε_D^F and ε_S^F in the formation strain
 422 (Roeloffs, 2010; Hodgkinson *et al.*, 2013):

$$\begin{aligned}
 & \begin{pmatrix} \text{Re}(e_1^{M_2}) & \text{Im}(e_1^{M_2}) & \text{Re}(e_1^{O_1}) & \text{Im}(e_1^{O_1}) \\ \text{Re}(e_2^{M_2}) & \text{Im}(e_2^{M_2}) & \text{Re}(e_2^{O_1}) & \text{Im}(e_2^{O_1}) \\ \text{Re}(e_3^{M_2}) & \text{Im}(e_3^{M_2}) & \text{Re}(e_3^{O_1}) & \text{Im}(e_3^{O_1}) \\ \text{Re}(e_4^{M_2}) & \text{Im}(e_4^{M_2}) & \text{Re}(e_4^{O_1}) & \text{Im}(e_4^{O_1}) \end{pmatrix} \\
 423 & \\
 424 & = \mathbf{C} \begin{pmatrix} \text{Re}((\varepsilon_A^F)^{M_2}) & \text{Im}((\varepsilon_A^F)^{M_2}) & \text{Re}((\varepsilon_A^F)^{O_1}) & \text{Im}((\varepsilon_A^F)^{O_1}) \\ \text{Re}((\varepsilon_D^F)^{M_2}) & \text{Im}((\varepsilon_D^F)^{M_2}) & \text{Re}((\varepsilon_D^F)^{O_1}) & \text{Im}((\varepsilon_D^F)^{O_1}) \\ \text{Re}((\varepsilon_S^F)^{M_2}) & \text{Im}((\varepsilon_S^F)^{M_2}) & \text{Re}((\varepsilon_S^F)^{O_1}) & \text{Im}((\varepsilon_S^F)^{O_1}) \end{pmatrix}, \quad (\text{B1})
 \end{aligned}$$

425 where $\text{Re}(e_i^{M_2})$ and $\text{Im}(e_i^{O_1})$ denote the real amplitude of the measured tidal strain
 426 M₂ and the imaginary amplitude of the measured tidal strain O₁ in the *i*-th gauge of the
 427 borehole strainmeter, respectively. $\text{Re}((\varepsilon_A^F)^{M_2})$ and $\text{Im}((\varepsilon_A^F)^{O_1})$ denote the real
 428 amplitude of the M₂ tides and the imaginary amplitude of the O₁ tides in the modeled
 429 formation strain ε_A^F , respectively.

430 The unknown parameters in matrix **C** are determined by minimizing the difference
 431 D between the measured M₂/O₁ amplitude ratios e_i^k and the predicted
 432 amplitudes $(e_i^k)^{\text{pred}}$ using equation (B1):

$$433 \quad D = \left(\sum_{i=1}^4 \sum_{k=M_2, O_1} \left(\frac{(\text{Re}(e_i^k) - \text{Re}(e_i^k)^{\text{pred}})^2}{\text{Re}(e_i^k)^2} + \right. \right.$$

434
$$\frac{(\text{Im}(e_i^k) - \text{Im}(e_i^k)^{\text{pred}})^2}{\text{Im}(e_i^k)^2} \Big)^{\frac{1}{2}} \quad (\text{B2})$$

435 We used the Nelder-Mead downhill simplex method (Nelder & Mead, 1965) to find the
 436 minimum D and optimal unknown parameters $C^1 - C^4$, $D^1 - D^4$, and $H^1 - H^4$.
 437 The three strain gauges are sufficient to compute the three components of the formation
 438 strain field (Hart *et al.*, 1996; Roeloffs, 2010; Hodgkinson *et al.*, 2013), and the fourth
 439 gauge provides redundancy to allow a self-consistency test (Roeloffs, 2010).

440 In this study, we estimated five sets of calibration coefficients: a set to estimate the
 441 three components of the formation strain field using all four strain gauges and four sets
 442 using any three of the four strain gauges (1, 2, and 3; 1, 2, and 4; 1, 3, and 4; and 2, 3 and
 443 4). These sets of calibration coefficients allow us to judge whether an observed anomalous
 444 strain change is caused by a change in the regional strain or by a local change and/or an
 445 instrument problem by comparing the four formation stress field estimates. For any three
 446 of the four gauges, ($i, j, k = 1, 2, 3$ or 4):

447
$$\begin{pmatrix} e_i \\ e_j \\ e_k \end{pmatrix} = \mathbf{C} \begin{pmatrix} \varepsilon_A^F \\ \varepsilon_D^F \\ \varepsilon_S^F \end{pmatrix}, \quad (\text{B3})$$

448
$$\mathbf{C} = \begin{pmatrix} C^i & (D^i \cos 2\varphi_i - H^i \sin 2\varphi_i) & (D^i \sin 2\varphi_i + H^i \cos 2\varphi_i) \\ C^j & (D^j \cos 2\varphi_j - H^j \sin 2\varphi_j) & (D^j \sin 2\varphi_j + H^j \cos 2\varphi_j) \\ C^k & (D^k \cos 2\varphi_k - H^k \sin 2\varphi_k) & (D^k \sin 2\varphi_k + H^k \cos 2\varphi_k) \end{pmatrix} \quad (\text{B4})$$

449 The optimal calibration coefficients in \mathbf{C} are estimated by the same procedure using
 450 equation (B1) and minimizing D in equation (B2) to calibrate the four gauges.

451

452

453 Appendix C Synthetic seismic strain wave calculation by normal-mode summation

454 Synthetic seismic waves excited by a point source in a non-rotating, self-

455 gravitational, spherically symmetric Earth can be calculated by normal-mode

456 summation (Gilbert & Dziewonski, 1975; Dziewonski *et. al.*, 1981). Using Aki &

457 Richards (1980)'s notation, the displacement field $\mathbf{u}(\mathbf{x}, t)$ excited by a moment tensor

458 time series $M(t)$ is:

$$\begin{aligned} 462 \quad \mathbf{u}(\mathbf{x}, t) = \sum_i [{}_i\bar{e}_{pq}(x_s)M_{pq}\dot{}(t)] \\ 463 \quad * {}_i\mathbf{u}(\mathbf{x}) \left(\frac{1 - \exp(-\omega_i t/2Q_i)\cos\omega_i t}{\omega_i^2} \right) \quad (C1) \end{aligned}$$

459 where i represents the mode number, the terms in the first set of parentheses correspond

460 to excitation terms, the terms in the second set of parentheses represent the decaying

461 oscillation of the i -th mode, and the asterisk * denotes convolution.

464 Since the wavelength of the eigenmode of interest in this study is much longer than

465 the sensor installation depth, the sensor depth can be regarded as zero.

466 Using spherical coordinates (r, Δ, \varnothing) where r is the radial distance from the

467 Earth's center, and Δ and \varnothing are the co-latitude and longitude measured from the point

468 source. The strain tensor components $e_{\Delta\Delta}$, $e_{\varnothing\varnothing}$, $e_{\Delta\varnothing}$ and e_{vol} , observable by borehole

469 strainmeters, are spatial derivatives of the displacement. They can be represented as

470 follows:

$$\begin{aligned}
 471 \quad & e_{\Delta\Delta} \\
 472 \quad & = \frac{1}{r} \frac{\partial u_{\Delta}}{\partial \Delta} \\
 473 \quad & + \frac{u_r}{r} \tag{C2}
 \end{aligned}$$

$$474 \quad e_{\phi\phi} = \frac{1}{r \sin \Delta} \frac{\partial u_{\phi}}{\partial \phi} + \frac{u_{\Delta}}{r} \cot \Delta + \frac{u_r}{r} \tag{C3}$$

$$478 \quad e_{\Delta\phi} = \frac{1}{2} \left[\frac{1}{r} \left(\frac{\partial u_{\phi}}{\partial \Delta} - u_{\phi} \cot \Delta \right) + \frac{1}{r \sin \Delta} \frac{\partial u_{\Delta}}{\partial \phi} \right] \tag{C4}$$

$$479 \quad e_{vol} = e_{rr} + e_{\Delta\Delta} + e_{\phi\phi} = \frac{\partial u_r}{\partial r} + e_{\Delta\Delta} + e_{\phi\phi} \tag{C5}$$

475 Equations (C2) - (C5) are represented by the following formulas in terms of the
 476 radial eigenfunctions ${}_n U_l$, and ${}_n V_l$ for the spherical mode and ${}_n W_l$ for the toroidal mode,
 477 and the fully normalized spherical harmonic functions Y_l^m (Aki & Richards, 1980),

$$\begin{aligned}
 480 \quad e_{\Delta\Delta} &= \frac{1}{r} {}_n U_l Y_l^m \\
 481 \quad &+ \frac{1}{r} \sqrt{\frac{1}{l(l+1)}} {}_n V_l \frac{\partial^2 Y_l^m}{\partial \Delta^2} \\
 482 \quad &+ \frac{1}{r} \sqrt{\frac{1}{l(l+1)}} im {}_n W_l \left(\frac{1}{\sin \Delta} \frac{\partial Y_l^m}{\partial \Delta} - \frac{\cos \Delta}{\sin^2 \Delta} Y_l^m \right) \tag{C6}
 \end{aligned}$$

$$\begin{aligned}
 483 \quad e_{\phi\phi} &= \frac{1}{r} {}_n U_l Y_l^m \\
 484 \quad &+ \frac{1}{r} \sqrt{\frac{1}{l(l+1)}} \left(\cot \Delta \frac{\partial Y_l^m}{\partial \Delta} - m^2 \frac{1}{\sin^2 \Delta} Y_l^m \right) {}_n V_l \\
 485 \quad &+ \frac{1}{r} \sqrt{\frac{1}{l(l+1)}} im \left(\frac{\cos \Delta}{\sin^2 \Delta} Y_l^m - \frac{1}{\sin \Delta} \frac{\partial Y_l^m}{\partial \Delta} \right) {}_n W_l \tag{C7}
 \end{aligned}$$

$$486 \quad e_{\Delta\phi} = \frac{1}{r} \sqrt{\frac{1}{l(l+1)}} im \left(\frac{1}{\sin \Delta} \frac{\partial Y_l^m}{\partial \Delta} - \frac{\cos \Delta}{\sin^2 \Delta} Y_l^m \right) {}_n V_l$$

487
$$-\frac{1}{r} \sqrt{\frac{1}{l(l+1)}} \left(\frac{\partial^2 Y_l^m}{\partial \Delta^2} + \frac{l(l+1)}{2} Y_l^m \right) {}_n W_l \quad (\text{C8})$$

488
$$e_{vol} = \left(\frac{2}{r} {}_n U_l + \frac{d {}_n U_l}{dr} - \frac{1}{r} \sqrt{l(l+1)} {}_n V_l \right) Y_l^m \quad (\text{C9})$$

489 where summation notations are omitted, and only the middle term of (C1) is represented
 490 for simplicity. n , l and m are the radial, co-latitudinal and azimuthal wave numbers for
 491 the eigenmodes, respectively. Only $|m| \leq \min(l, 2)$ concerns the point source (Aki &
 492 Richards, 1980).

493 We developed the computer program “synthe_me” which can calculate synthetic
 494 horizontal strain tensors based on equations (C1) - (C9). This program adopts the
 495 eigenfunctions calculated by the computer program OBANI (Woodhouse, 1988) using
 496 the PREM Earth model with the ocean. The computer program can also calculate
 497 synthetic displacement vectors and tilt vectors. The synthetic seismograms of long-
 498 period strain calculated by this computer program was already verified by comparing
 499 with strains observed by the extensometer at Matsushiro and the volumetric strainmeter
 500 at Gamagori for the 2004 Sumatra-Andaman earthquake and the 2005 Nias earthquake
 501 (Kamigaki et al., 2009).

502

503

504 **References**

- 505 Agnew, D.C., 1996. SPOTL: Some programs for ocean-tide loading. in SIO Ref. Ser.96-8,
506 35pp. Scripps Institution of Oceanography, La Jolla, CA.
- 507 Agnew, D.C., 1997. NLOADF: A program for computing ocean-tide loading, Journal of
508 Geophysical Research, 102, 5109-5110.
- 509 Aki, K. & Richards, P.G., 1980. Quantitative Seismology, Theory and Methods, vol.1,
510 W.H.Freeman and Co., San Francisco, CA.
- 511 Ando, M., 1975. Source Mechanisms and Tectonic Significance of Historical Earthquakes along
512 Nankai Trough, Japan, Tectonophysics, 27, 119-140.
- 513 Asai, Y., Ishii, H. & Aoki, H., 2009. Comparison of tidal strain changes observed at the
514 borehole array observation system with in situ rock properties in the Tono region, central
515 Japan, Journal of Geodynamics, 48, 292-298.
- 516 Berger, J. & Beaumont, C., 1976. Analysis of Tidal Strain Observations from United-States-of-
517 America .2. Inhomogeneous Tide, B Seismol Soc Am, 66, 1821-1846.
- 518 Dziewonski, A.M. & Anderson, D.L., 1981. Preliminary reference Earth model Phys Earth
519 Planet In, 25, 297-356.
- 520 Dziewonski, A.M., Chou, T.A. & Woodhouse, J.H., 1981. Determination of earthquake source
521 parameters from waveform data for studies of global and regional seismicity, Journal of
522 Geophysical Research, 86, 2825-2852.
- 523 Ekström, G., Nettles, M. & Dziewonski, A.M., 2012. The global CMT project 2004-2010:
524 Centroid-moment tensors for 13,017 earthquakes, Phys Earth Planet In, 200, 1-9.
- 525 Gilbert, F., 1980. An Introduction to Low-frequency Seismology. in Physics of the Earth's
526 Interior, Proc. 'Enrico Fermi' International School of Physics, eds. Dziewonski, A. M. &
527 Boschi, E. North Holland Publ. Co., Amsterdam.

528 Gladwin, M.T., 1984. High precision multi component borehole deformation monitoring,
529 Review of Scientific Instruments, 55, 2011–2016.

530 Gladwin, M.T. & Hart, R., 1985. Design Parameters for Borehole Strain Instrumentation, Pure
531 and Applied Geophysics, 123, 59 - 80.

532 Hart, R.H.G., Gladwin, M.T., Gwyther, R.L., Agnew, D.C. & Wyatt, F.K., 1996. Tidal
533 calibration of borehole strain meters: Removing the effects of small-scale inhomogeneity,
534 Journal of Geophysical Research, 101, 25553-25571.

535 Hodgkinson, K., Langbein, J., Henderson, B., Mencin, D. & Borsa, A., 2013. Tidal calibration
536 of plate boundary observatory borehole strainmeters, Journal of Geophysical Research:
537 Solid Earth, 118, 447-458.

538 Ishii, H., Yamauchi, T., Matsumoto, S., Hirata, Y. & Nakao, S., 2002. Development of Multi-
539 component Borehole Instruments for Earthquake Prediction Study: Some Observed
540 Examples of Precursory and Co-seismic Phenomena Relating to Earthquake Swarms and
541 Application of the Instrument for Rock Mechanics in Seismogenic Process Monitoring,
542 eds. Ogasawara, H., Yanagidani, T. & Ando, M. A.A. Balkema Publishers, Lisse, the
543 Netherlands.

544 Itaba, S., Koizumi, N., Matsumoto, N. & Ohtani, R., 2010. Continuous Observation of
545 Groundwater and Crustal Deformation for Forecasting Tonankai and Nankai Earthquakes
546 in Japan, Pure and Applied Geophysics, 167, 1105-1114.

547 Kamigaichi, O., Matsumoto, N. and Hirose, F., 2020, Modified GOTIC2: Software for
548 estimation of tidal loading effects at subsurface observation. GSJ Open-File Report, no.
549 705, 1 CD-ROM, Geol. Surv. Japan, AIST, available in
550 <https://www.gsj.jp/data/openfile/no0705/openfile0705indexEN.html>, accessed 27 May
551 2021.

552 Kamigaichi, O., Matsumoto, N. and Hirose, F. 2021, Green's function at depth of borehole
553 observation required for precise estimation of the effect of ocean tidal loading near coasts,
554 Geophysical Journal International, in press.

555 Kamigaki, T., Ikegami, Y., Nakanishi, I., Kokubo, K., Tsuyuki, T., Nakamura, K. and Harada,
556 S., 2009, Analysis of long-period strain seismograms for great far earthquakes:2004
557 Sumatra-Andaman earthquake (Mw.9.0) and 2005 Nias earthquake, Geophysical Bulletin
558 of Hokkaido University, 72, 379-382.

559 King, G. C. P., Zürn, W., Evans, R., and Emter, D., 1976, Site correction for long-period
560 seismometers, tiltmeters, and strainmeters, *Geophys. J. Roy. Astron. Soc.*, 44, 405-411.

561 Kitagawa, Y., Itaba, S., Matsumoto, N. & Koizumi, N., 2011. Frequency characteristics of the
562 response of water pressure in a closed well to volumetric strain in the high-frequency
563 domain, *Journal of Geophysical Research*, 116, doi:10.1029/2010JB007794.

564 Koizumi, N., 2013. Earthquake prediction research based on observation of groundwater -
565 Earthquake forecasting based on crustal deformation estimated from groundwater level
566 change -, *Synthesiology -English edition*, 6, 27-37.

567 Matsumura, S., Murakami, M. & Imakiire, T., 2004, Concept of the New Japanese Geodetic
568 System, *Bulletin of the Geographical Survey Institute*, 51, 1-9.

569 Nelder, J.A. & Mead, R., 1965. A Simplex-Method for Function Minimization, *Comput J*, 7,
570 308-313.

571 Obara, K. & Hirose, H., 2006. Non-volcanic deep low-frequency tremors accompanying slow
572 slips in the southwest Japan subduction zone, *Tectonophysics*, 417, 33-51.

573 Obara, K., Hirose, H., Yamamizu, F. & Kasahara, K., 2004. Episodic slow slip events
574 accompanied by non-volcanic tremors in southwest Japan subduction zone, *Geophysical
575 Research Letters*, 31.

576 Park, J., Amoruso, A., Crescentini, L. & Boschi, E., 2008. Long-period toroidal earth free
577 oscillations from the great Sumatra-Andaman earthquake observed by paired laser
578 extensometers in Gran Sasso, Italy, *Geophysical Journal International*, 173, 887-905.

579 Roeloffs, E., 2010. Tidal calibration of Plate Boundary Observatory borehole strainmeters:
580 Roles of vertical and shear coupling, *Journal of Geophysical Research*, 115.

581 Sato, T. & Harrison, J.C., 1990. Local-Effects on Tidal Strain-Measurements at Esashi, Japan,
582 *Geophysical Journal International*, 102, 513-526.

583 Sekine, S., Hirose, H. & Obara, K., 2010. Along-strike variations in short-term slow slip events
584 in the southwest Japan subduction zone, *Journal of Geophysical Research*, 115.

585 Tamura, Y., Sato, T., Ooe, M. & Ishiguro, M., 1991. A Procedure for Tidal Analysis with a
586 Bayesian Information Criterion, *Geophysical Journal International*, 104, 507-516.

587 Wessel, P. & Smith, W.H.F., 1998. New, improved version of generic mapping tools released,
588 *Eos, Transactions American Geophysical Union*, 79, 579-579.

589 Woodhouse, J.H., 1988. IV.2 The calculation of the eigenfrequencies and eigenfunctions of the
590 free oscillations of the earth and the sun. in *Seismological Algorithms*, pp. 321–370, ed.
591 Doornbos, D. J. Academic Press, London.

592 Zürn, W., Ferreira, A.M.G., Widmer-Schmidrig, R., Lentas, K., Rivera, L. & Clévéde, E., 2015.
593 High-quality lowest-frequency normal mode strain observations at the Black Forest
594 Observatory (SW-Germany) and comparison with horizontal broad-band seismometer data
595 and synthetics, *Geophysical Journal International*, 203, 1786-1803.

596 Figure and Table Captions

597

598 Figure 1 Observatory locations. Black rectangles show the locations of Ishii-type
599 borehole strainmeters deployed after 2007. Light blue rectangles show GTSM locations.

600 The green circle (TYE) shows the location of the Ishii-type borehole strainmeter

601 deployed in 2004. Red dots indicate slow earthquakes determined by the Japan

602 Meteorological Agency.

603

604 Figure 2 Schematic illustration of observatory with Ishii-type borehole strainmeter.

605 Each observatory has three observation wells and an observation hut. GNSS stations are

606 deployed in some observatories.

607

608 Figure 3 Schematic illustrations of strain-gauge orientation (0, 45, 90 and 135

609 degrees) for Ishii-type borehole strainmeters and GTSMs.

610

611 Figure 4a Theoretical and observed strains derived from surface waves produced by

612 2010 Chile (Maule) earthquake. The travel time of the phases of the seismic waves in

613 ANO are given in Kitagawa *et al.* (2011).

614

615 Figure 4b Theoretical and observed strains derived from surface waves produced by 2010
616 Chile (Maule) earthquake.

617

618 Figure 4c Theoretical and observed strains derived from surface waves produced by 2010
619 Chile (Maule) earthquake.

620

621 Table 1 Locations of observation stations, deployment depths of borehole
622 strainmeters, depths for calculating Green's function, lithology at the deployment depths
623 and azimuths of channel 1 for borehole strainmeters. Information for the 11 Ishii-type
624 strainmeters is given in Kamigaichi et al. (2021).

625

626 Table 2 Extracted tidal responses for the M_2 and O_1 tidal components and the
627 atmospheric responses from the 15 borehole strainmeter data. Phases are relative to the
628 local tidal potential, and negative phase values indicate lag. These responses of the 11
629 Ishii-type strainmeters are given in Kamigaichi et al. (2021).

630

631 Table 3 Predicted tidal strains at the deployment depth at the observation stations

632 estimated using the modified GOTIC2 program. Phases are relative to the local tidal
633 potential, and negative phase values indicate lag. These tidal strains for the 11 Ishii-type
634 strainmeters are given in Kamigaichi et al. (2021). r_d is the horizontal distance from
635 the observatory to the coast.

636

637 Table 4 Calibration matrices \mathbf{C} , coupling matrices \mathbf{K} , and \mathbf{D} derived from equation
638 (B2), D_{matrix} calculated from equation (A8), and perturbation matrices \mathbf{P} for the fifteen
639 borehole strainmeters.

640 Supporting Information for
641 Tidal Calibration of Multicomponent Borehole Strainmeters and Validation of the
642 Method Using Surface Waves

643 Norio Matsumoto* and Osamu Kamigaichi*,**

644

645 * Geological Survey of Japan, National Institute of Advanced Industrial Science and
646 Technology (AIST)

647 ** Japan Meteorological Business Support Center

648

649 **Figures S1a-S1l**

650 Theoretical and observed strains derived from surface waves produced by 2010 Chile
651 (Maule) earthquake.

652

Figures

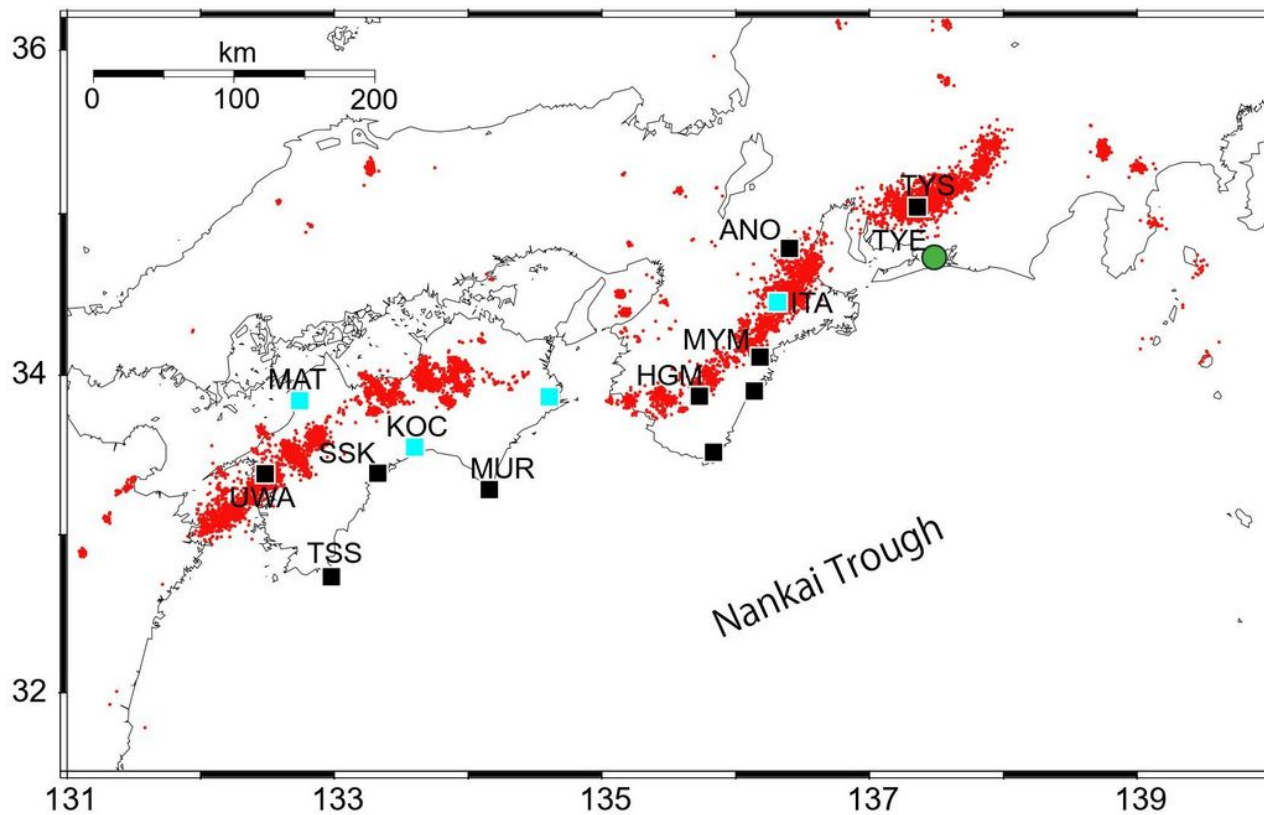


Figure 1

Observatory locations. Black rectangles show the locations of Ishii-type borehole strainmeters deployed after 2007. Light blue rectangles show GTSM locations. The green circle (TYE) shows the location of the Ishii-type borehole strainmeter deployed in 2004. Red dots indicate slow earthquakes determined by the Japan Meteorological Agency.

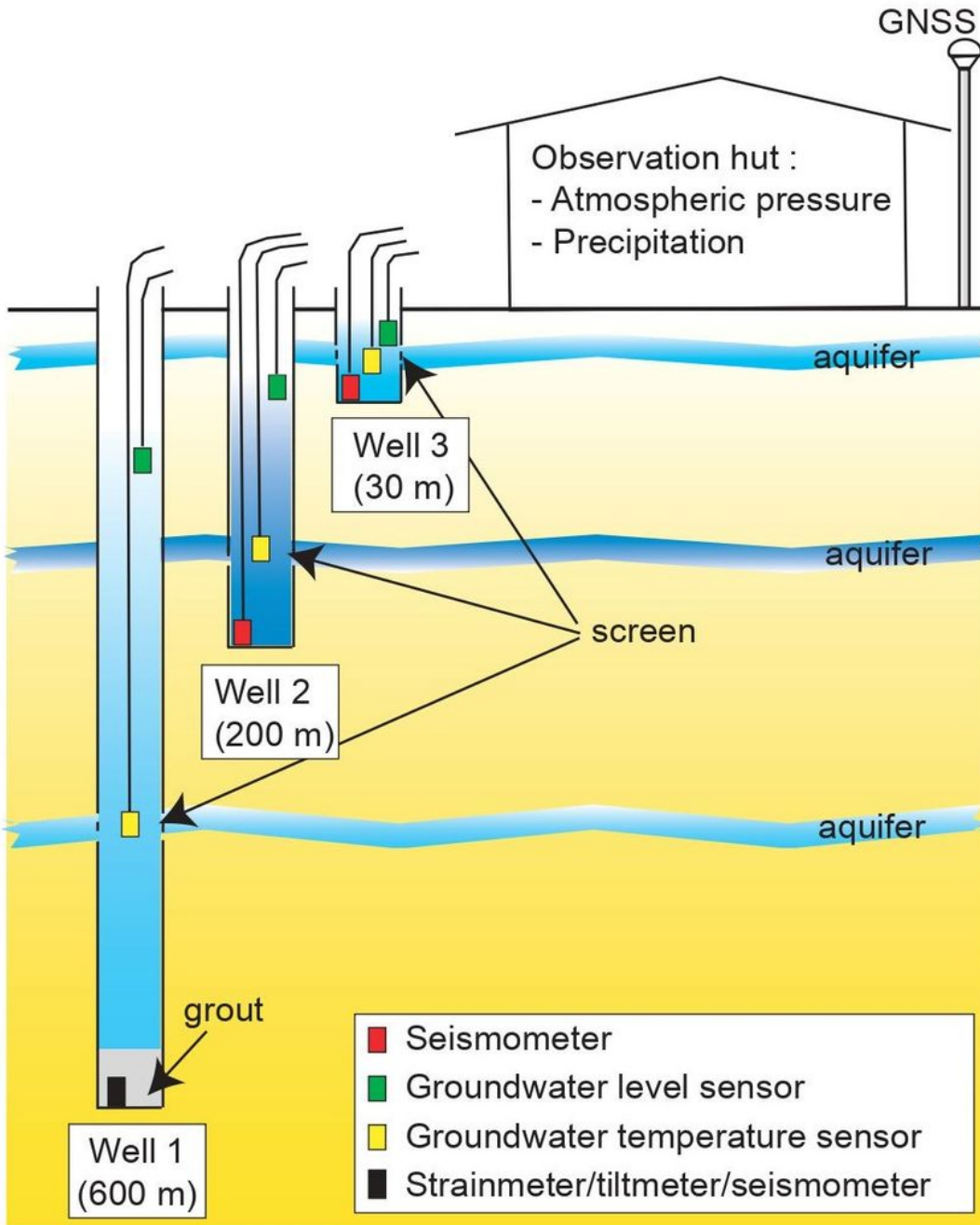


Figure 2

Schematic illustration of observatory with Ishii-type borehole strainmeter. Each observatory has three observation wells and an observation hut. GNSS stations are deployed in some observatories.

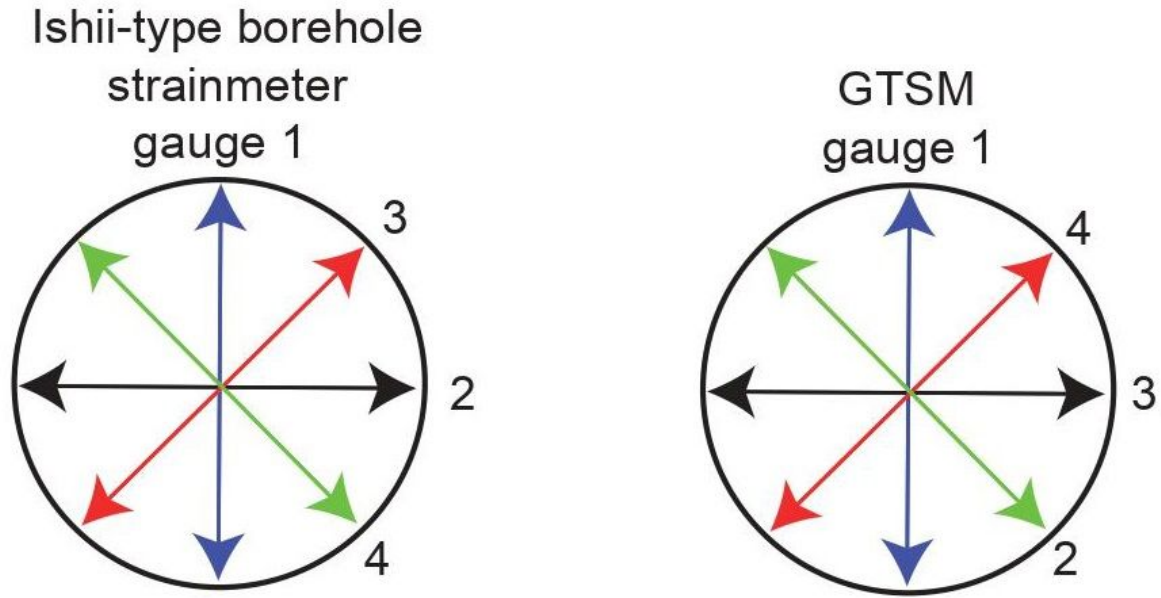


Figure 3

Schematic illustrations of strain-gauge orientation (0, 45, 90 and 135 degrees) for Ishii-type borehole strainmeters and GTSMs.

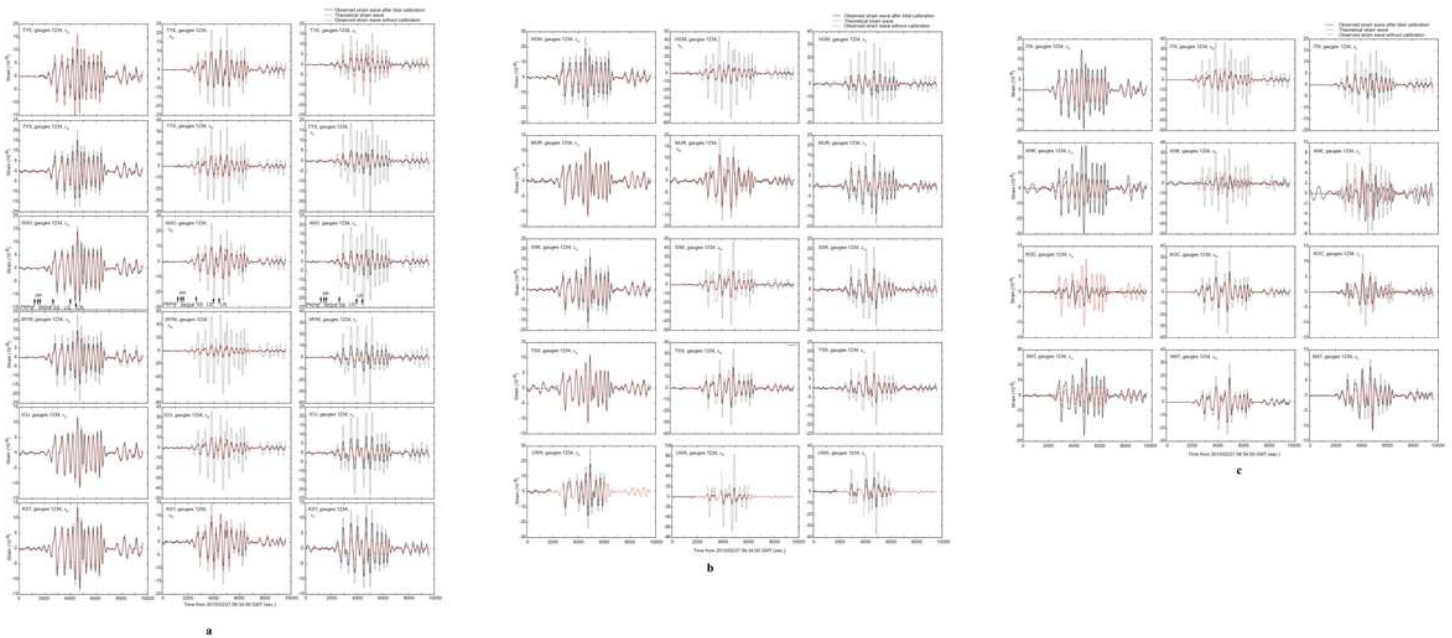


Figure 4

4a Theoretical and observed strains derived from surface waves produced by 2010 Chile (Maule) earthquake. The travel time of the phases of the seismic waves in ANO are given in Kitagawa et al.

(2011). 4b Theoretical and observed strains derived from surface waves produced by 2010 Chile (Maule) earthquake. 4c Theoretical and observed strains derived from surface waves produced by 2010 Chile (Maule) earthquake.

Supplementary Files

This is a list of supplementary files associated with this preprint. Click to download.

- [Table1.jpg](#)
- [Table2.png](#)
- [Table3.jpg](#)
- [Table4.png](#)
- [matsumotoetalelectricabstract.jpg](#)
- [matsumotoetalsupfigs20210607.pdf](#)